UNIVERSITY OF CALIFORNIA SAN DIEGO

Numerical Modeling of Fluid-driven Hydraulic Fracturing and *J*-integral Analysis

A thesis submitted in partial satisfaction of the requirements for the degree

Master of Science

in

Structural Engineering

by

Shijun Wei

Committee in charge:

Professor Ingrid Tomac, Chair
Professor Veronica Eliasson
Professor John S. McCartney

2020

The Thesis of Shijun Wei is approved, and it is acceptable in quality and form for publication on microfilm and electronically:

_____

_____

_____

Chair

University of California San Diego

2020

TABLE OF CONTENTS

LIST OF FIGURES

LIST OF TABLES

ACKNOWLEDGEMENTS

I would like to express the sincere appreciation to my committee chair, Dr. Ingrid Tomac, who continuously and convincingly guide me throughout the research. Without her guidance and patient help, this thesis would not have been possible.

I would also like to thank my committee members, Dr. Veronica Eliasson and Dr. John S. McCartney for providing necessary revising and supplementing suggestions to enhance the performance of this thesis.

Finally, enormous love to my family, friends, and colleagues. Your motivation and support are crucial along the way.

ABSTRACT OF THE THESIS

Numerical Evaluation of Inelastic Hydraulic Fracture Propagation in Georeservoirs with *J*-Integral Analysis

by

Shijun Wei

Master of Science in Structural Engineering

University of California San Diego, 2020

Professor Ingrid Tomac, Chair

This paper numerically investigates inelastic behavior of sandstone for better understanding of hydraulic fracture propagation in georeservoirs. Although many numerical, theoretical, and experimental studies investigated hydraulic fracturing, not enough emphasis has

been given to the inelastic behavior of rock prior and during the hydraulic fracture propagation. Current practice widely uses linear elastic fracture mechanics (LEFM) principles for prediction of hydraulic fracturing in weak sandstone. However, discrepancies between LEFM models and filed or laboratory results indicate presence of plastic deformation, such as are for example micro-cracks or acoustic emission cloud data. Therefore, this study uses *J*-integral for obtaining hydraulic fracture propagation criteria under the elastic-plastic stress-strain state. *J*-integral is calculated on the path around a DEM model in two-dimensions. A synthetic rock mass modeled in DEM has an advantage of time-stepping and stress-strain redistribution which leads to micro-cracks represented by broken bonds between DEM particles, and therefore models well elastoplastic behavior. The relationship between far-field stress magnitudes and breakdown pressures, process zone length and calculated *J*-integral values are presented. The relationship between crack driving forces and applied stresses is investigated to better understand the plasticity effects. The influence of stiffness of sandstone on breakdown pressures and *J*-integral values are also studied. Overall, results show that LEFM is not applicable for describing fracture propagation at higher confinement stresses. Inelastic *J*-integral increases dramatically with rock confinement, especially its plastic portion.

CHAPTER 1: INTRODUCTION

Hydraulic fracturing is a commonly used technique to simulate the fracking process mostly in low permeability rocks. The process is typically generated by injecting fluid like water, chemical solution, and sand into rocks via wells under high pressures; and the process is intended to create new fractures or enlarge existing fractures, which finally reaches to breakdown. Breakdown is known as a complex process, and breakdown pressure is an important rate-dependent, size-dependent, and fracture-fluid-dependent parameter obtained during hydraulic fracturing stress measurements. Early developments of hydraulic fracturing modeling included two-dimensional and three-dimensional versions with linear elasticity assumptions (Yew 1997; Khristianovic and Zheltov 1955; Perkins and Kern 1961; Clifton and Abou-Sayed 1981; Valkó and Economides 1995; Economides and Boney 2000). Recent developments of hydraulic fracturing simulators focus on bridging multiscale problems and interaction between natural existing fractures and hydraulic induced fractures as a system, using the Discrete Fracture Network (DFN) model and unconventional fracture model (UFM) (Yang et al. 2018; Damjanac et al. 2010; Meyer and Bazan 2011; Kresse et al. 2013). Stress shadowing of existing fractures is introduced in the Discrete Fracture Network (DFN) for modeling interaction between fracture branches and their effect on fracture propagation direction (Kresse et al. 2013). Extended finite element method (XFEM) has been also used widely for modeling hydraulic fracture propagation (Lecampion 2009; Chen 2013; Qingwen, Yuwen, and Tiantang 2009; Gordeliy and Peirce 2013). A step forward towards modeling more realistic crack propagation was recently done by introducing a cohesive zone model and poroelasticity to XFEM for modeling fracture propagation in porous rock mass (Liu et al. 2017; Vahab and Khalili 2018; Wang 2015; Carrier and Granet 2012). However, the cohesive zone model, which is valid for concrete and rocks, is also used within the framework of LEFM

because it assumes that the cohesive zone is small compared to the fracture length (Irwin 1957). To conclude, all the existing hydraulic fracturing models still rely on LEFM solutions. In practical applications of hydraulic fracturing, the measured net pressures are usually higher than those predicted by models (Shlyapobersky 1985). It has been argued that higher net pressures are due to better than expected containment, poor measurement of closure stress, near-wellbore effects, complex fracturing, poor understand of rheology, and rock heterogeneity and nonlinearity. Crack tip effects can lead to scale effect on fracture toughness for field size fractures. The un-wetted zone in front of the crack tip has lower pressure than the close pressure and can clamp the fracture tip to locally reduce the stress intensity in the rock. At the shallow depth hydraulic fracturing experiment, sizable fluid leg zones were found (Warpinski et al. 1985). The possibility of large damage zone and plasticity around the fractur tip may invalidate the LEFM.

In the context of this paper, elastic-plastic fracture mechanics is applied for the study to capture the time-dependent and nonlinear behavior of weak sandstone. *J*-integral has been selected as the main inelastic fracture criterion to study the crack-tip conditions during elastic-plastic behavior in hydraulic fracturing.

CHAPTER 2: METHODOLOGY

2.1. Discrete Element Method

Discrete Element Method (DEM) has been introduced by Cundall and Strack and has been widely used in the chemical, mining, and civil engineering fields (Cundall and Strack 1979). DEM solves dynamic motions of particulate assembly by using an explicit finite difference scheme. Individual particle behavior is represented by constant velocities and accelerations for each timestep and the calculation is done in DEM by applying Newtown's second law to particles and force-displacement law to contacts. Compared to commonly used continuum methods, DEM has the advantage of better tracking fractures and simulating crack propagation through explicit modeling of micro-cracks as broken shear and tensile bonds between DEM particles, which are essential in studying hydraulic fracturing problems. This study uses Particle Flow Code, known as PFC, which implemented DEM framework to simulate the dynamic movements and interactions between particles within granular systems (Itasca, 2018). Synthetic rock modeled in PFC is represented by an assembly of balls and bonds with specified stiffness and strength. The particles, visualized as disks in two-dimensional model and spheres in three-dimensional model, are treated as rigid bodies that can translate and rotate independently with respect to each other.

The bonded particle model (BPM) is adopted in PFC to create bonding for selected contacts within assemblies, and BPM involves contact-bonded models (CBM), parallel-bonded models (PBM), flat-jointed models (FJM), and smooth-jointed models (SJM). Despite that parallel-bonded models are more universally used for rock behavior simulation, two-dimensional flat-jointed models (FJM) are used here, which first described by Potyondy (Potyondy 2012). FJM simulates contacts as the interface of two individual particles. This type of model overcomes the main

disadvantages of BPM, which yields low ratio of compressive to tensile rock strength and low friction angles. BPM has been found in the past to wrongly represent the rock parameters tested in the lab. FJM formulation consists of kinematics and force-displacement law. For kinematics, the total relative motion of the interface can be tracked by:

$$d_n = d_n + \Delta d_n \tag{1}$$

$$d_t = d_t + \Delta d_t \tag{2}$$

$$\theta = \theta + \Delta\theta \tag{3}$$

where d_n is the total relative displacement in normal direction, d_t is the total relative displacement in tangential direction, θ is the total relative rotation, and Δ denotes increments of each. The incremental relative displacements and rotations can also be calculated within a given timestep by:

$$\Delta d = \Delta d_n \hat{\boldsymbol{n}}_{\boldsymbol{c}} + \Delta d_t \hat{\boldsymbol{t}}_{\boldsymbol{c}} \tag{4}$$

$$\Delta d = (\dot{d}_n \Delta t)\hat{\boldsymbol{n}}_{\boldsymbol{c}} + (\dot{d}_t \Delta t)\hat{\boldsymbol{t}}_{\boldsymbol{c}} \tag{5}$$

$$\Delta\theta = \Delta\theta\hat{\boldsymbol{k}} = (\dot{\theta}\Delta t)\hat{\boldsymbol{k}} \tag{6}$$

where Δd_n is the incremental relative motion in normal direction, Δd_t is the incremental relative motion in tangential direction, $\Delta\theta$ is the incremental relative rotation, $\dot{d}_n$ is the relative translational velocity in normal direction, $\dot{d}_t$ is the relative translational velocity in tangential direction, $\dot{\theta}$ is the relative rotational velocity, $\hat{\boldsymbol{n}}_{\boldsymbol{c}}$ is the unit normal vector at contact point, $\hat{\boldsymbol{t}}_{\boldsymbol{c}}$ is the unit tangential vector at contact point, $\hat{\boldsymbol{k}}$ is the unit vector in vertical direction to the motional plane, and Δt is the specified calculation timestep. The interface gap of two dimensional FJM can be calculated as follow when the system is expressed in ξ system

$$g(\xi) = d_n + \theta(\xi - \bar{R}) \tag{7}$$

where $\bar{R}$ is the half length of particle contact surfaces. The gap g_0 between two particles is defined positive for an open gap and negative for overlap. Small angle approximation is also applied so that $\tan(\theta) \approx \theta$. Each contact surface is equally divided into *N* segments, and each segment will generate a force, $F^{(e)}$ and a moment, $M^{(e)}$ at the centroid. Therefore, each interface, which coincides with the contact, will carry a force F_c and a moment M_c calculated as follows:

$$F_c = \sum_{i=1}^{N} F^{(e)} \tag{8}$$

$$M_c = \sum_{i=1}^{N} \{\left(r^{(e)} \times F^{(e)}\right) + M^{(e)})\} \tag{9}$$

where *N* is the number of equal-length segments within one contact surface, and $r^{(e)}$ is the position vector for each segment. Figure 2.1 below shows the configuration of flat-jointed models around the contacts and force-moment calculation diagram.

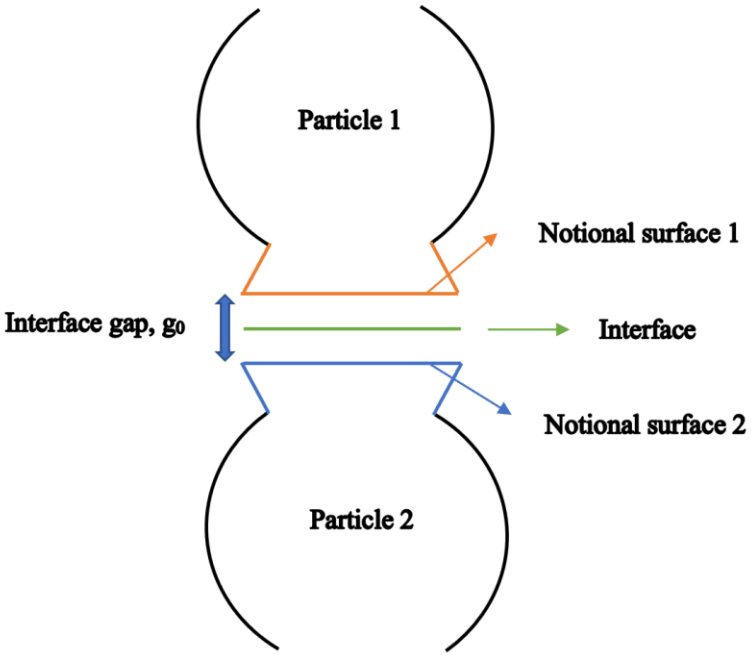

Figure 2.1. Flat-jointed model configuration

Breakdown pressure can be initially calculated from the maximum principal stress, the minimum principal stress, and the properties of the rock based on Kirsch solution. The expression is shown as follow:

$$P_b = 3\sigma_{h,\min} - \sigma_{H,\max} + \sigma_t - P_0 \quad (10)$$

where P_b is the calculated breakdown pressure at the borehole, $\sigma_{h,\min}$ is the minimum horizontal stresses, $\sigma_{H,\max}$ is the maximum horizontal stresses, σ_t is the tensile strength of the rock, and P_0 is the initial pore pressure exist in the specimen.

2.2. Hydro-mechanical coupling and *J*-integral calculation

PFC adopts the theory of Cundall's algorithm in simulating the fluid flow [Cundall 2000]. The simulation is done by assuming each contact point of particles formulates a flow channel, and these channels connect to reservoirs, which store fluids as well as generate hydraulic pressures. For each channel, there is a specific aperture associated based on the following equation:

$$a = \frac{a_0\sigma_0}{\sigma+\sigma_0} \quad (11)$$

where a is the aperture for each channel, a_0 is the residual aperture that pre-existing at the time particles are just in touch, σ_0 is the contact stress at which the aperture halves, and σ is the normal compressive stress at the contact between particles. For flow rate, parallel plates condition is assumed and the equation for calculating the rate of fluid flow through channels are listed as follow:

$$Q = \frac{a^3\Delta P}{12\mu L} \quad (12)$$

where Q is the rate of fluid through channels by assuming parallel plates condition, ΔP is the change in pressure across channels, μ is the fluid dynamic viscosity, and L is the length of the channels. Fluid pressures are induced by pumping fluids into the specimen via fluid reservoirs at

borehole. Due to fluid flow in channels, pressures change in reservoirs at each time-step, and impose pressure forces locally to the surrounding DEM particles, which creates a hydro-mechanical coupling process. The pressures in each reservoir and the forces acting on each DEM particle are updated at each timestep Δt; and the change in pressures within each fluid reservoir can be calculated as follows:

$$\Delta P = \frac{K_f}{V}(\sum Q\,\Delta t - \Delta V_d) \tag{13}$$

where K_f is the fluid bulk modulus, V is the volume of the fluid, ΔV_d is the change in volume of the fluid reservoir, and $\sum Q$ is the sum of volumetric flow received for each fluid reservoir in a given timestep. Table 2.1 below shows the parameters used for fluid simulation.

Table 2.1. Parameters for fluid flow simulation

ap_zero (mm^2)	1.0	*bulk_w* (GPa)	2.15
gap_mul	0.4	*flow_dt* (s)	10^{-6}
F_{ap_zero} (MPa)	20	*delvol* (mm^3)	16.5

(Note: *ap_zero* = initial residual aperture, *gap_mul* = gap multiplier, F_{ap_zero} = contact stress at which the aperture halves, *bulk_w* = bulk modulus for the fluid, *flow_dt* = flow timestep, *delvol* = change of volume per step)

Rice (1968) extended linear elastic methodology to elastic-plastic for better understanding the fracture behavior in nonlinear materials. Rice applied deformation plasticity to study the cracks in nonlinear materials and showed that *J*, which referred to the nonlinear energy release rate, can be written as path-independent line integral (Rice 1968). In the case of analyzing elastic-plastic *J*-

integral, the calculation of *J* is computed by the addition of both elastic and plastic components as follows:

$$J_{tot} = J_{el} + J_{pl} \tag{14}$$

For the calculation of *J* in this study, the results from PFC are outputted into MATLAB, and the definition of path independent integral *J* introduced by Rice is used for later crack analysis. The expression is shown here:

$$J = \int_{\tau}(W d_y - \vec{T} \cdot \frac{\overrightarrow{\partial_u}}{\partial_x} d_s) \tag{15}$$

where τ is any arbitrary contour surrounding the crack tip, and the direction of τ is defined in counterclockwise, W is the strain energy density, $\vec{T}$ is the traction on τ, and $\overrightarrow{\partial_u}$ is the displacement along the arc *s*. Boom and Shih et al. also showed that the *J*-integral solution can be plotted in FAD, known as Failure Assessment Diagrams [Bloom 1980]. The conversion from the applied *J* to an equivalent K_J can be done using the following equation:

$$K_J = \sqrt{\frac{JE}{1-\upsilon^2}} \tag{16}$$

where K_J is the crack driving force, *J* is the energy release rate, *E* is the Young's modulus of the specimen, and υ is the Poisson's ratio. The shape of the FAD curve is a function of plasticity effects, and *J* solution yields a more accurate description of FAD curve.

2.3. Model parameters calibration

To simulate the reasonable weak sandstone behavior and macro-parameters of the specimen, a calibration process is conducted so that the results from inputted micro-parameters match the physical properties. For creating a sample with flat-joint contacts, all existing contacts

are assumed to have certain micro properties. Three tests are proceeded listed as tension test, uniaxial test, and biaxial test. The specific values of micro-mechanical properties, micro stiffness to balls and micro strength of bonds in specific, are listed in Table 2.2. Biaxial test results are shown in Figure 2.2. In addition, the corresponding macro-mechanical properties are summarized in Table 2.3 getting from tests run results in PFC.

Table 2.2. Micro-parameters for flat-joint model

fj_ten	2.2 MPa	*fj_n*	2
fj_coh	21.0 MPa	*emod*	1.0 GPa
fj_fa	38.0°	*kratio*	2.5
fj_fric	0.3	G_{bond}	0.3 mm

(Note: *fj_ten* = flat joint tensile strength , *fj_coh* = flat joint cohesion, *fj_fa* = flat joint friction angle, *fj_fric* = flat joint friction coefficient, *fj_n* = number of elements in radial direction, *emod* = flat joint effective modulus, *kratio* = normal to shear stiffness ratio, G_{bond} = bond gap)

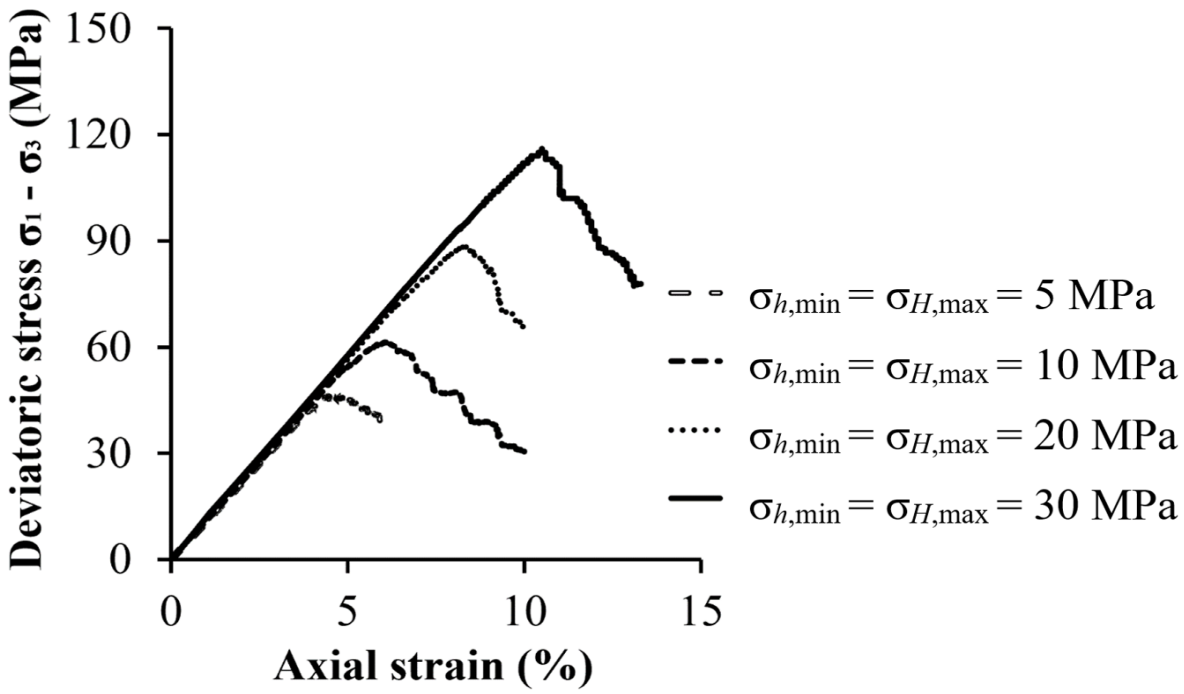

Figure 2.2. Biaxial test results in calibration process

Table 2.3. Macro properties for flat-joint model compared to the average values of sandstone from various sources. (Bandyopadhyay and Abdullah, 2013; Gercek, 2007; Park, 2006)

	PFC^{2D}	Weak sandstone
Tensile strength, σ_t (MPa)	1.7	0.9 – 3.8
Young's modulus, E (GPa)	1.1	1.6
Uniaxial compression strength, σ_c (MPa)	15.4	6 - 21
Fracture toughness ($MPa \cdot m^{1/2}$)	0.2	0.05 – 1.45
Poisson's ratio, ν (-)	0.2	0.05 - 0.4

2.4. Sample generation and measurements

Two-dimensional model is built in PFC with dimensions 5 x 10 cm. The origin of coordinate system is set at the center of the specimen, as the x-axis in horizontal direction and y-axis in vertical direction. Figure 2.3 shows a visualization of the geometry of the specimen and the applied boundary conditions.

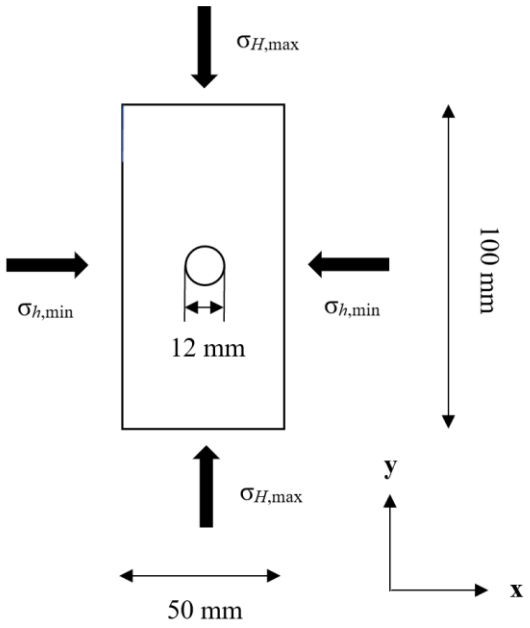

Figure 2.3. Geometry and boundary conditions of the model

The total number of DEM particles is around 3200 for each assembly. For matching the physical properties of the sandstone, the damping ratio is set to be 0.7, and density is set to be 2350 kg/m^3. The boundaries are created as walls along the four edges of the specimen. Circular borehole with radius of 6 mm is modeled after the application of the far field biaxial compressive stress field on outer boundaries. Table 2.4 summarizes the boundary conditions for simulation of hydraulic fracturing.

Table 2.4. Boundary conditions for hydraulic fracturing simulation

$\sigma_{h,\min}$ (MPa)	5 - 25	Injection filed *x* (cm)	-0.2 – 0.2
$\sigma_{H,\max}$ (MPa)	10 - 35	Injection filed *y* (cm)	-0.2 – 0.2

In terms of the stress and strain measurements of walls, reaction forces on opposites walls are averaged and divided by the representative area of the walls in each direction to return the horizontal and vertical stresses. To verify the results computed by the measure logic, two other approaches of computing stresses are provided: '*compute_spherestress(rad)*' and '*compute_averagestress*'. The results showed that the measure logic is precise enough within allowable tolerance. For strain measurement of walls, the measure logic is to evaluate the strain rate at a given step over a measurement region. Strain increments, therefore, can be accumulated at each iteration by using the computed value of the strain times the current timestep. Also, verification is provided by evaluating strain based on measuring relative displacements between gauge particles.

CHAPTER 3: RESULTS

Three studies are conducted in this paper. Studies focus on specific confining cases and reveal how the fracture, borehole pressure, and *J*-integral value changes with respect to time and fracture propagation. For one study, five different states are selected for testing listed as reaching the breakdown pressure, halfway between the breakdown pressure and peak pressure, reaching the peak pressure, halfway between the peak pressure and the end of the simulation, and reaching the end of the simulation. For each state, fracture pictures, borehole pressures, process zone length, and *J*-integral values are recorded for later analysis. Fracture behavior pictures are obtained from PFC, which are colored in red. Based on the results, crack length and process zone length can be easily captured; for better understanding the trends, both crack length and process zone length are plotted versus model running time so that it can be seen more visually that how these quantities change with time.

3.1. Effects of breakdown pressure interpretation

The exact point where the breakdown pressure occurs is still a matter of debate in the hydraulic fracturing community. Traditionally, the breakdown pressure coincides with the peak pressure measured at the borehole, which is supposed to occur at the same time as the fracture initiates. However, this micromechanical study, as well as, some previous experimental data, indicate the fracture initiation occurring somewhere in-between theoretical value from elastic Kirsch solution and the peak. *J*-integral is computed for five stages of borehole pressure, for the case of hydraulic fracturing of a sample with confinement of 5 MPa in *x*-direction and 10 MPa in *y*-direction. The following figure shows the plot of borehole pressure against model running time for all five points, and each is labelled in the corresponding location.

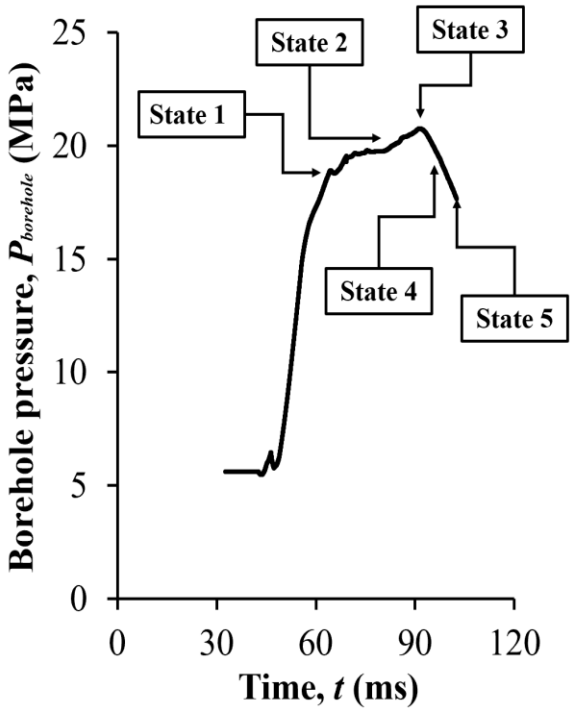

Figure 3.1. Borehole pressure histories versus running time ($\sigma_{h,\min}$=5.0 MPa and $\sigma_{H,\max}$=5.0 MPa)

For each point, two different contours are chosen to measure the *J* values, and the calculated *J* is the average of the two measurements. Figure 3.2 shows the fracture behaviors and *J* calculation contours, where the contours are chosen slightly different for each case for avoiding intersection with the major fractures.

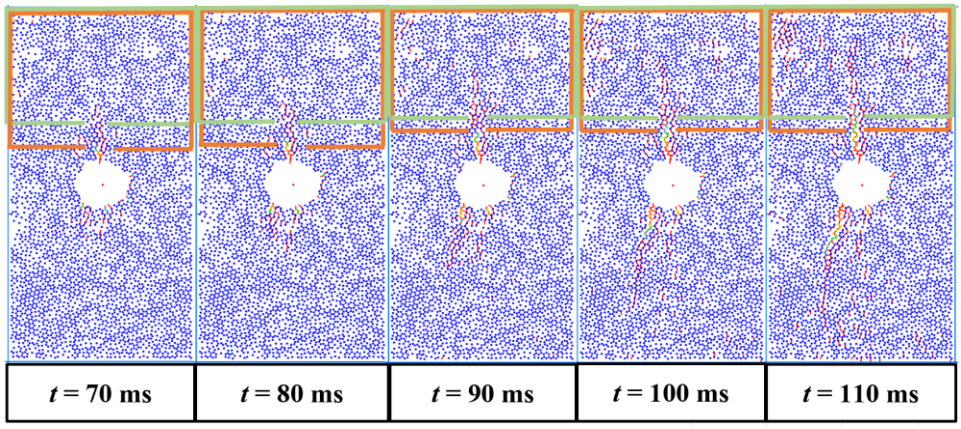

Figure 3.2. The fracture behavior pictures and contours ($\sigma_{h,\min}$=5.0 MPa and $\sigma_{H,\max}$=5.0 MPa)

The borehole pressure is measured using PFC history *BHpress*, and the values are recorded in Table 3.1.

Table 3.1. *J* value and borehole pressure calculation ($\sigma_{h,\min}$ =5.0 MPa and $\sigma_{H,\max}$=10.0 MPa)

State number	1	2	3	4	5
t (ms)	70	80	90	100	110
$P_{borehole}$ (MPa)	19.6	19.9	20.7	19.4	17.6
J (Pa·m)	288.5	255.4	268.6	268.8	267.2
J_{el} (Pa·m)	38.4	38.4	38.4	38.4	38.4
J_{pl} (Pa·m)	250.1	217.0	230.2	230.4	228.8
Increase of J from J_{el} (%)	651.3	565.1	599.5	600.0	595.8

As the results show, the borehole pressures are varying between 17.6 MPa and 20.7 MPa. According to the occurrence of the first visible microcrack, that 19.6 MPa is referring to the breakdown pressure at borehole, and 20.7 MPa is referring to the peak borehole pressure. This model confirms a discrepancy between real and assumed breakdown pressure, where the actual breakdown pressure is around 5% smaller than the peak values. *J*-integral elastic and plastic values J_{el} (elastic portion of *J*) and J_{pl} (plastic portion of *J*) values are obtained by calculating elastic portion from theoretical equation and then subtracting it from the total value to estimate the plastic part, shown in Table 3.1. It can be seen that plastic portion of *J*-integral is prevalent and up to six times larger than elastic portion, which coincides with the observation of irreversible deformation via microcracks in the model. The process zone, which is defined as unwetted zone in front of the fracture, is measured from the model and listed in Table 3.2. The total fracture length increased with time as expected; however, the observation suggested that the process zone lengths remains constant. To better see the changes of borehole pressures, process zone length, and *J* integral values

as the time runs from state 1 to state 5, Figure 3.3 and Figure 3.4 are plotted as a visualization of the results.

Table 3.2. Fracture length estimation ($\sigma_{h,\min}$ = 5 MPa and $\sigma_{H,\max}$ = 10 MPa)

Running time (ms)	70	80	90	100	110
Estimated fracture length (mm)	11.0	12.0	16.0	16.5	20.0
Estimated process zone length (mm)	8.50	8.75	10.75	9.00	10.25

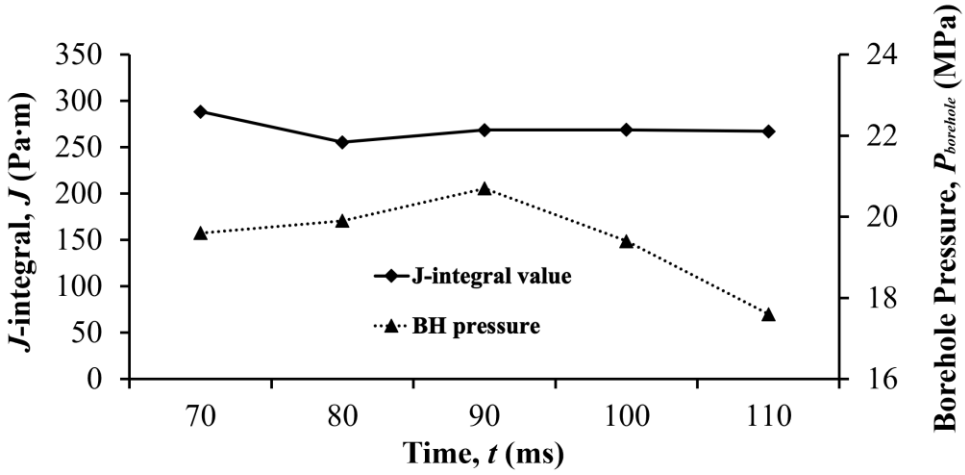

Figure 3.3. *J*-integral values and borehole pressure change with respect to running time

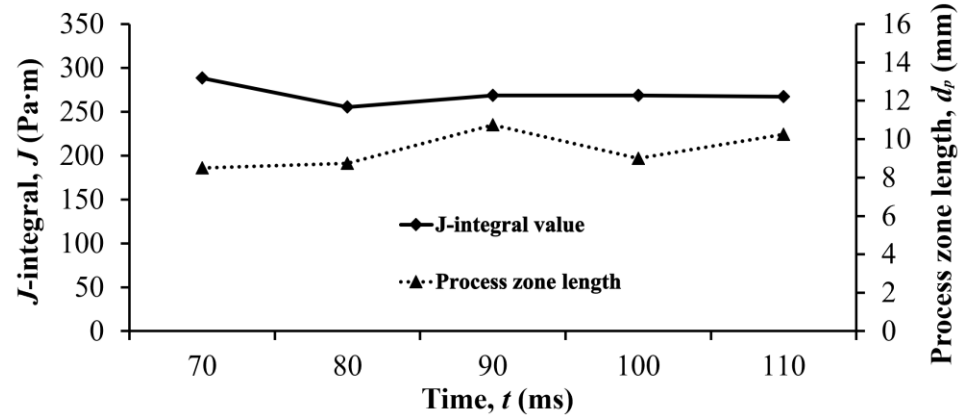

Figure 3.4. Process zone length change with respect to running time

3.2. Effects of confinement stress magnitudes

Effect of different confining stresses magnitudes is studied to better understand dependence of *J*-integral on the state of stress, which corresponds to different depths of reservoirs. Six different confining cases are tested and run, where Table 3.3 presents the confining pressures for each loading case, the calculated breakdown pressures from Kirsch solution and the breakdown pressures obtained from PFC as well as the peak values. The plots of borehole pressure versus model running time for each run are outputted from PFC and replotted in Figure 3.5.

Table 3.3. Six loading cases and breakdown pressures

Run number	$\sigma_{h,\min}$ (MPa)	$\sigma_{H,\max}$ (MPa)	P_b (MPa) (Kirsch solution)	P_b (MPa) (PFC)	P_{peak} (MPa) (PFC)
1	5	10	6.68	18.2	20.7
2	7	14	8.68	20.6	23.2
3	10	20	11.68	25.4	28.2
4	15	25	21.68	33.6	35.4
5	20	30	31.68	41.8	44.2
6	25	35	41.68	51.0	54.6

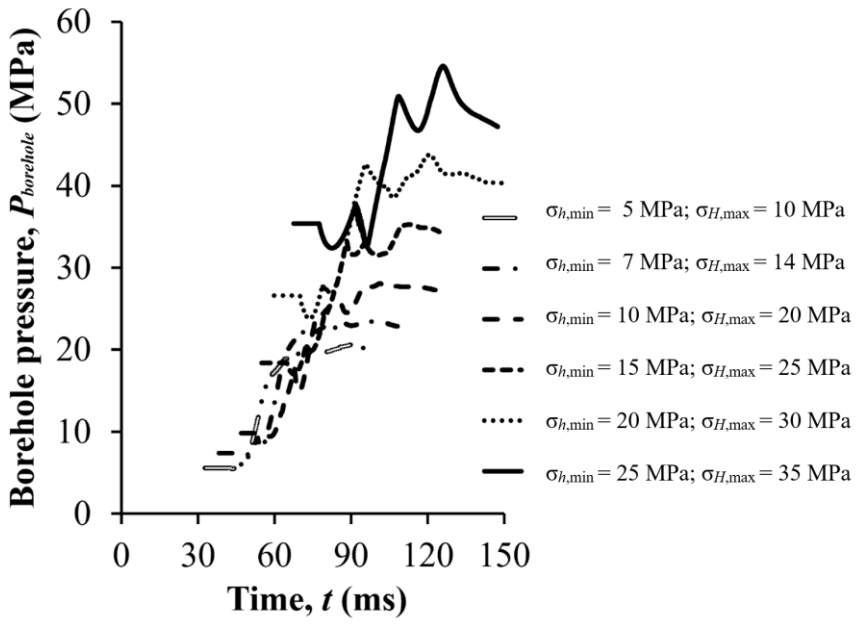

Figure 3.5. Borehole pressure histories versus running time for six cases

The fracture behaviors and contours are drawn in Figure 3.6. Lower confining stresses yield slightly more branching of the process zone. *J*-integral calculation contour is shown for each case as the green line. Quantities are shown in Table 3.4. With confinement increase, *J*-integral value dramatically rises, and the plastic *J* also rises being six times larger than elastic part for lower confinement and up to 82 times larger for maximum considered confinement. *J*-integral values indicate importance of considering inelastic behavior during hydraulic fracture propagation, especially when higher confinement pressures occur.

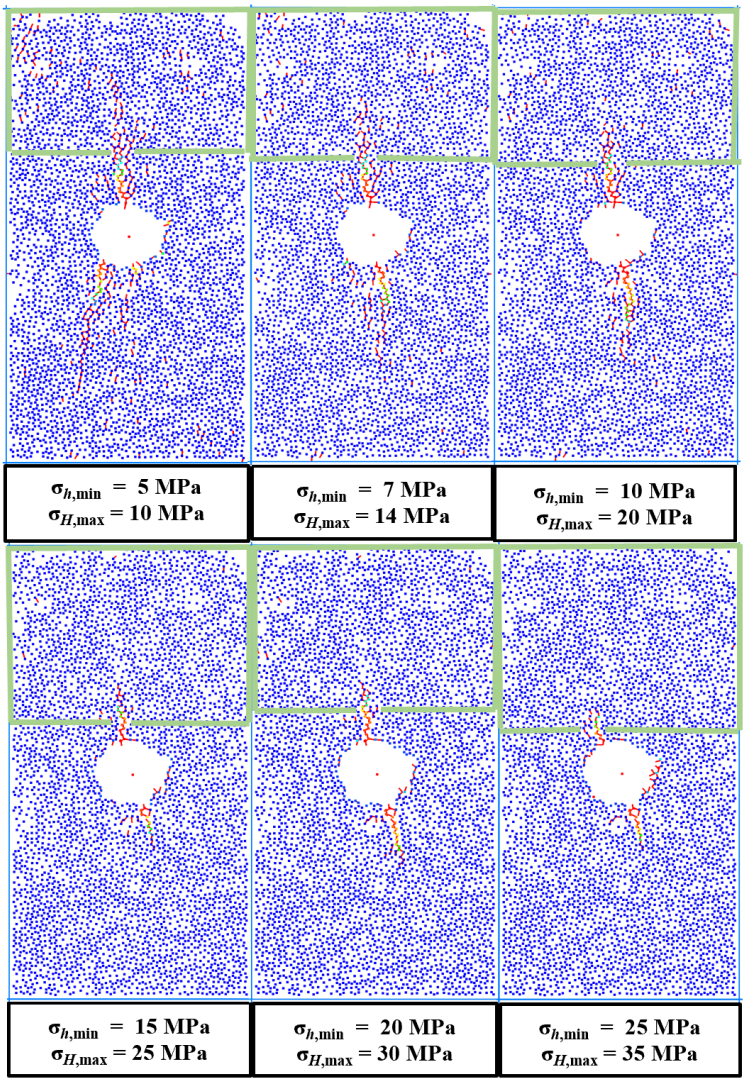

Figure 3.6. The fracture micromechanics for all six cases

Red to blue dots represent fluid reservoirs pressures, red lines are tensile broken bonds between particles, and green line is the *dS*, the *J*-integral calculation contour.

The calculation of J, J_{el}, J_{pl} values are listed in Table 8.

Table 3.4. *J*-integral value calculations for six cases

Run number	1	2	3	4	5	6
$\sigma_{h,\min}$ (MPa)	5	7	10	15	20	25
$\sigma_{H,\max}$ (MPa)	10	14	20	25	30	35
J (Pa·m)	268.8	502.6	988.5	1607.9	2498.3	3220.5
J_{el} (Pa·m)	38.4	38.4	38.4	38.4	38.4	38.4
J_{pl} (Pa·m)	230.4	464.2	950.1	1569.5	2459.9	3182.1
Increase of J from J_{el} (%)	600.0	1208.9	2474.2	4087.2	6406.0	8286.7

In terms of process zone length, the results are presented in Table 3.5. As the confining pressures increase, the process zone length for each case decreases by a large amount.

Table 3.5. Fracture length estimation for six cases

Run number	1	2	3	4	5	6
$\sigma_{h,\min}$ (MPa)	5	7	10	15	20	25
$\sigma_{H,\max}$ (MPa)	10	14	20	25	30	35
Estimated fracture length (mm)	16.5	15.8	12.0	9.25	8.25	5.25
Estimated process zone length (mm)	9.00	8.55	4.50	3.00	1.50	0.75

Plots is created as Figure 3.7 to better capture the quantified relationship between breakdown pressures versus *J*-integral values. Increase in the breakdown pressure, which occurs because of increased depths and far-field compressive stresses, is accompanied with the increase in *J*-integral value.

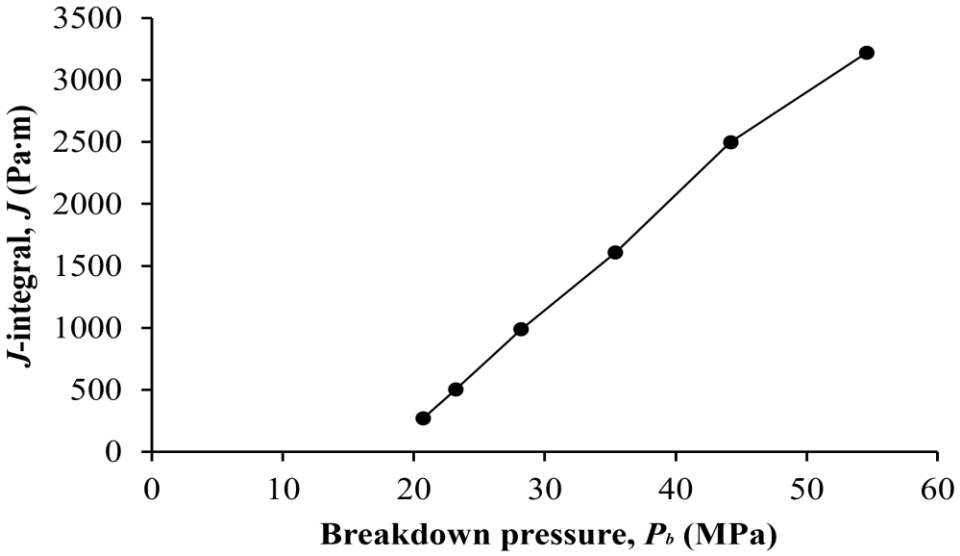

Figure 3.7. The relationship between breakdown pressure P_b and J values

Based on the results from J-integral values, crack driving forces are calculated and plotted against breakdown pressures, the minimum horizontal pressures $\sigma_{h,\min}$ and the maximum horizontal pressures $\sigma_{H,\max}$ shown in Figure 3.8. The results show a significant increase in apparent fracture toughness, which rises to be up to 7 times larger than at low confinement stress.

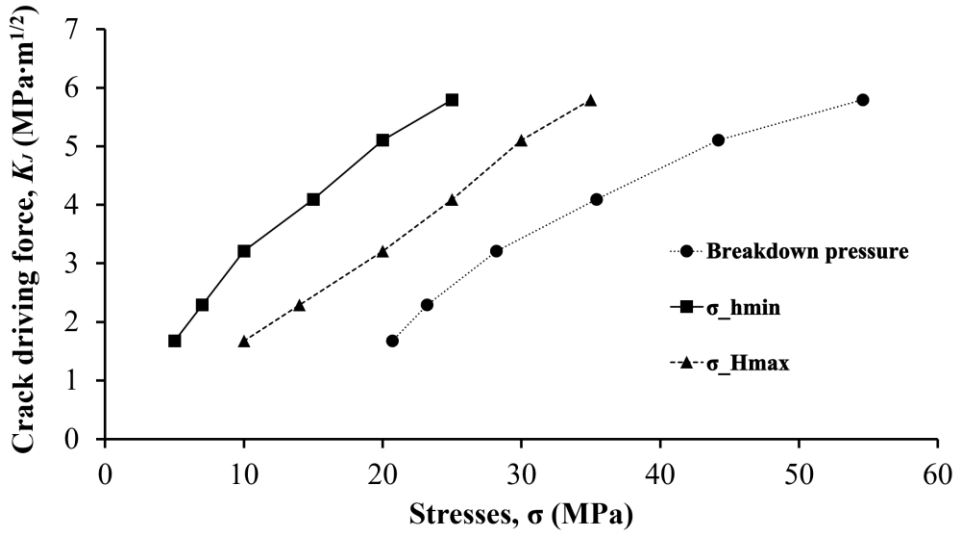

Figure 3.8. The relationship between crack driving force with stresses

3.3. Effects of confinement stress contrast

The contrast in confinement stress is studied in order to better understand if the differences in horizontal principal stresses affect the *J*-integral value for a certain case of constant vertical principal confinement stress, parallel with the borehole axis in the two dimensional case for this study. Table 3.6 below presents the confining cases for each run, calculated breakdown pressures based on Kirsch solution, recorded breakdown pressures from PFC, as well as peak pressures observed at the borehole, respectively. The fracture behaviors and *J*-integral measurement contours are drawn in Figure 3.9.

Table 3.6. Breakdown pressures and peak borehole pressures

for constant $\sigma_{h,\min}$ and different $\sigma_{H,\max}$

Run number	$\sigma_{h,\min}$ (MPa)	$\sigma_{H,\max}$ (MPa)	P_b (MPa) (Kirsch solution)	P_b (MPa) (PFC)	P_{peak} (MPa) (PFC)
1	10	12	19.68	23.2	27.0
2	10	14	17.68	24.8	28.8
3	10	17	14.68	26.0	28.9
4	10	18	13.68	26.2	29.0
5	10	19	12.68	25.2	28.0
6	10	20	11.68	25.4	28.2
7	10	22	9.68	25.2	27.2
8	10	24	7.68	24.4	26.8
9	10	26	5.68	26.0	27.4
10	10	28	3.68	25.6	27.2

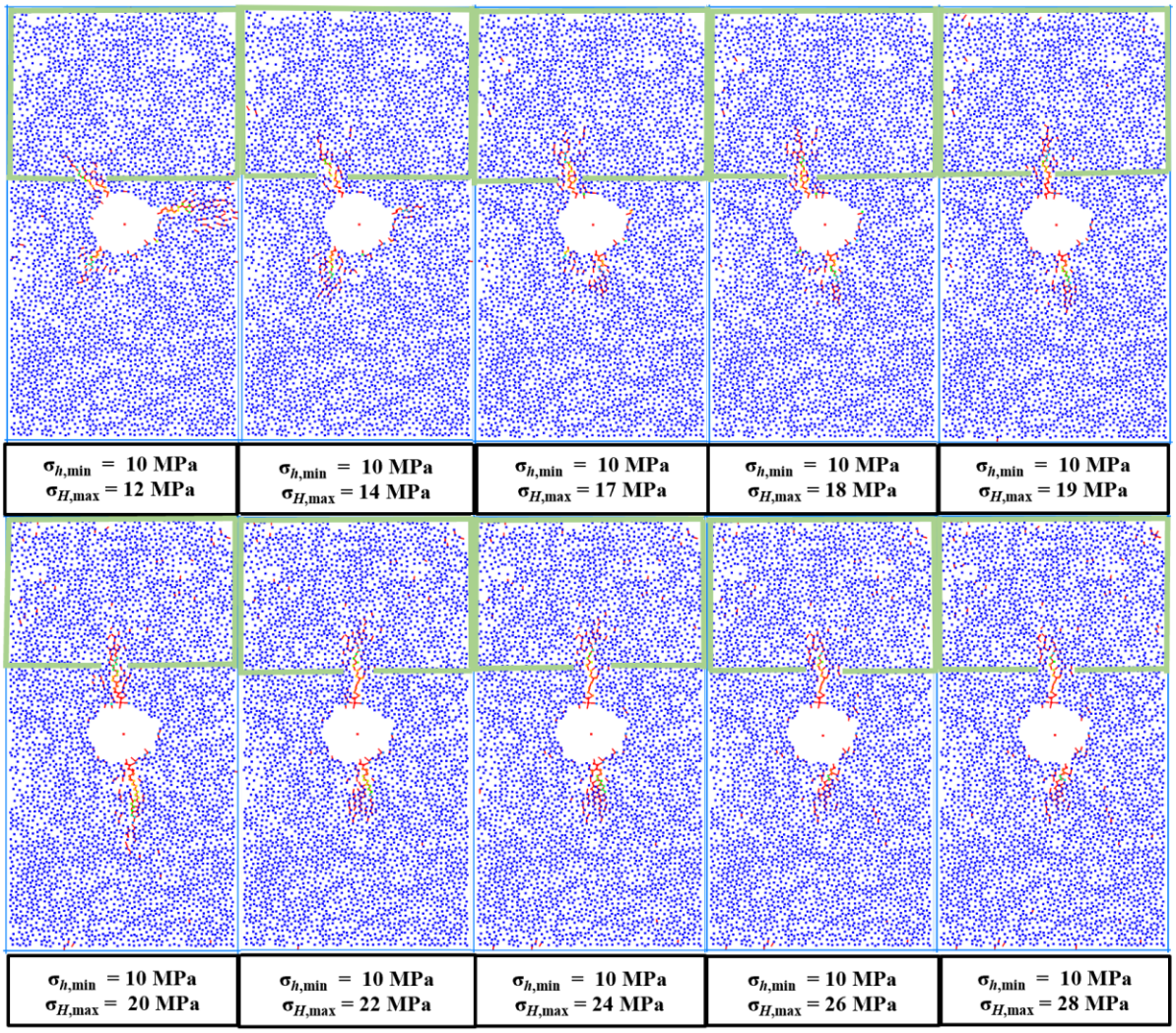

Figure 3.9. Fracture behaviors and contours for constant $\sigma_{h,\min}$ and different $\sigma_{H,\max}$

From the results shown in Table 3.6, the general relationship of calculated breakdown pressures based on Kirsch solution, the measured breakdown pressures from PFC, and the observed peak pressures at boreholes follow the similar trend as discussed in previous two studies. There is noticeable difference between predicted and measured breakdown pressures, and the peak pressures at borehole are slightly larger than the breakdown pressures. The following table shows the *J*-integral analysis results.

Table 3.7. *J*-integral value calculations for constant $\sigma_{h,\min}$ and different $\sigma_{H,\max}$

Run number	$\sigma_{h,\min}$ (MPa)	$\sigma_{H,\max}$ (MPa)	J (Pa·m)	J_{el} (Pa·m)	J_{pl} (Pa·m)	Increase of J from J_{el} (%)
1	10	12	739.6	38.4	701.2	1826.0
2	10	14	789.8	38.4	751.4	1956.8
3	10	17	798.6	38.4	760.2	1979.7
4	10	18	820.1	38.4	781.7	2035.7
5	10	19	869.4	38.4	831.0	2164.1
6	10	20	988.5	38.4	950.1	2474.2
7	10	22	1112.5	38.4	1074.1	2797.1
8	10	24	1284.1	38.4	1245.7	3244.0
9	10	26	1458.6	38.4	1420.2	3698.4
10	10	28	1666.0	38.4	1627.6	4238.5

It can be observed that as keeping the minimum horizontal confining stresses same, the *J*-integral increases as the maximum horizontal confining stresses increase. In addition, large amount of plastic deformation occurred as expected from previous two studies. The plastic portion of *J* is about 20 to 40 times larger than the elastic portion as *J* for this particular study. To better visualize the change of *J*-integral in terms of the increasing of $\sigma_{H,\max}$, plot below is presented as Figure 3.10.

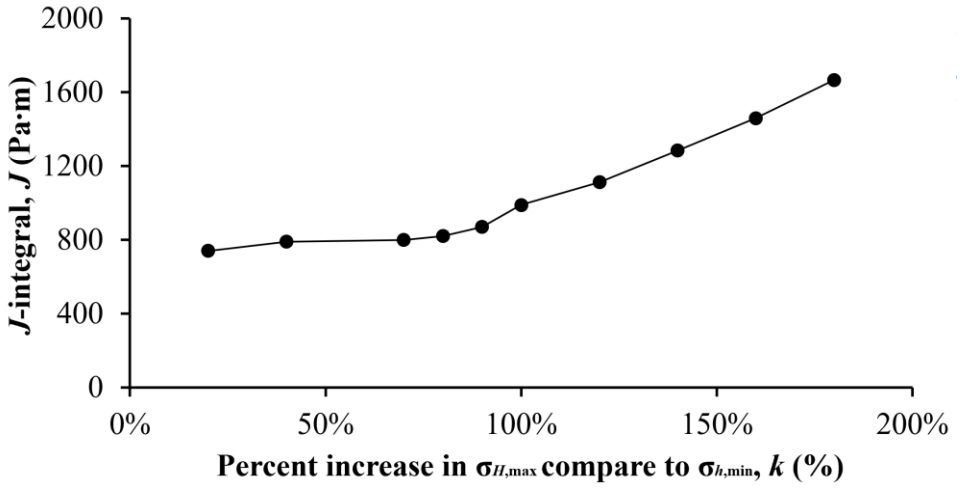

Figure 3.10. The relationship between *J*-integral and *k* (percent increase in $\sigma_{H,\max}$)

3.4. Effects of sandstone stiffness

Besides all the studies that conducted above, the effects of sandstone stiffness on *J*-integral values are also studied. For this particular study, two different Young's modulus (*E*) listed as 1 GPa and 5 GPa are chosen for the sandstone specimens. Similar procedures are proceeded to find the peak pressures and breakdown pressures at the borehole for six distinguish confining cases based on each sandstone stiffness model. Table 3.8 below summarizes the results for Young's modulus of sandstones at 5 GPa.

Table 3.8. Breakdown pressures and peak borehole pressures for E = 5 GPa

Run number	$\sigma_{h,\min}$ (MPa)	$\sigma_{H,\max}$ (MPa)	P_b (MPa) (Kirsch solution)	P_b (MPa) (PFC)	P_{peak} (MPa) (PFC)
1	5	10	6.68	23.0	24.7
2	7	14	8.68	28.2	31.0
3	10	20	11.68	32.4	35.5
4	15	25	21.68	43.8	47.0
5	20	30	31.68	55.0	60.9
6	25	35	41.68	55.2	63.5

As the values shown in Table 3.8, if compared to Table 3.3, it can be shown that at given confining pressures, the breakdown pressures at borehole increase as the stiffness of the sandstone increases.

Figure 3.11 below show the fracture behaviors of the samples and *J*-integral values evaluation contours.

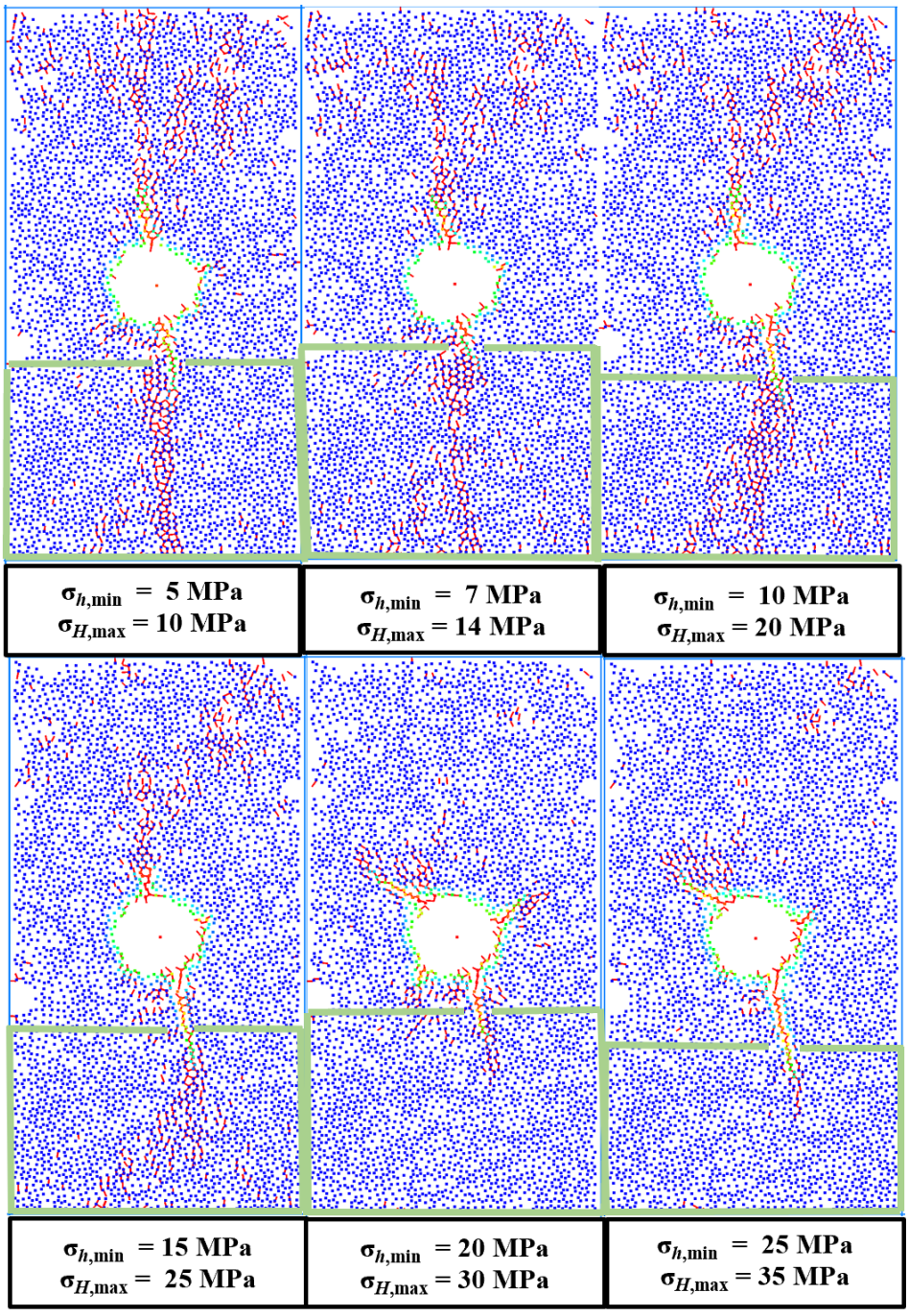

Figure 3.11. Fracture behaviors and contours for E = 5 GPa

The following table show the calculated J-integral analysis results for the two different sandstone stiffness 5 GPa.

Table 3.9. *J*-integral value calculations for E = 5 GPa

Run number	1	2	3	4	5	6
$\sigma_{h,\min}$ (MPa)	5	7	10	15	20	25
$\sigma_{H,\max}$ (MPa)	10	14	20	25	30	35
J (Pa·m)	358.0	789.2	1327.4	2519.5	3643.7	5706.8
J_{el} (Pa·m)	7.68	7.68	7.68	7.68	7.68	7.68
J_{pl} (Pa·m)	350.3	781.5	1319.7	2511.8	3636.0	5699.1
Increase of J from J_{el} (%)	4561.2	10175.8	17183.6	32705.7	47343.8	74207.0

From the results shown in Table 3.9, it can be recognized that large amount of plastic deformation occurred during fractures as expected from previous studies. For the sandstones with Young's modulus of 5 GPa, the plastic portion of J could increase as large as 740 times than the elastic portion of J for confining pressures of 25 MPa and 35 MPa.

CHAPTER 4: CONCLUSION

Hydraulic fracturing of sandstone is a topic relevant to oil, gas and geothermal reservoirs. Although hydraulic fracture initiation and propagation has been extensively studied experimentally, numerical approaches mostly rely on linear elastic fracture mechanics (LEFM). This study uses DEM to model hydraulic fracture propagation in two-dimensional model, where the synthetic rock parameters are matched well with a previously published laboratory studies regarding the material physical and mechanical parameters. Hydraulic fracture is initiated and propagated using a constant flow rate at a borehole, which is low enough to be quasi-static. Pressure drop is accompanied with fracture propagation typical for hydraulic fracturing in the field. DEM uses flat-jointed model (FJM) in the Particle Flow Code (PFC^{2D}) as the contact model which has been previously proven to well model tensile to compressive intact rock strength ratio. The models studied inelastic fracture behaviors before, at and after the peak borehole pressures, and under different far-field confining stresses. Admittedly, the model used in this study is still a simplification of the real rock mass conditions due to the two-dimensional interpretation and low resolution. However, this model can sufficiently demonstrate hydraulic fracturing behaviors and use to perform various analysis like identifying breakdown pressures, estimating process zone length, and measuring *J*-integral values for elastic-plastic conditions. In addition, the relation between these significant quantities can also be studied.

The breakdown pressures, process zone length, *J*-integral calculations, and crack-driving forces are calculated to better understand inelastic fracture propagation and to assess the applicability of LEFM.

Micromechanical analysis of hydro-mechanical fracture initiation and propagation from the borehole in biaxially compressed two-dimensional model showed that for lower confinements, the fracture initiates at approximately 5% lower value than the peak borehole pressure recorded at the borehole for quasi-static flow rates. *J*-integral value has been calculated at five points before, at the peak and after the peak. *J*-integral and stays approximately similar for all the cases. However, a plastic portion of *J*-integral is approximately 5-6 times larger than the elastic portion. Therefore, LEFM is an inadequate tool for predicting hydraulic fracturing.

With confinement increase, *J*-integral value dramatically rises, and the plastic *J* also rises being six times larger than elastic part for lower confinement and up to 82 times larger for maximum considered confinement. *J*-integral values indicate importance of considering inelastic behavior during hydraulic fracture propagation, especially when higher confinement pressures occur.

Increase in the breakdown pressure, which occurs because of increased depths and far-field compressive stresses, is accompanied with the increase in *J*-integral value. There is an inversely proportional relationship between process zone length and *J*-integral values, where the process zone decreases at higher confinement far-field stresses.

For constant minimum horizontal confining stresses, as the maximum horizontal confining stresses increase, the *J*-integral values increase correspondingly. The plastic portion of *J* is observed to be 18 times larger than the elastic portion of *J* for $\sigma_{h,\min}$ = 10 MPa and $\sigma_{H,\max}$ = 10 MPa; in comparison, the plastic of *J* is 42 times larger than the elastic portion of *J* for $\sigma_{h,\min}$ = 10 MPa and $\sigma_{H,\max}$ = 28 MPa.

For increasing the stiffness of sandstone, the observed peak pressures and breakdown pressures at the borehole are increasing as well. Unsurprisingly, large amount of plastic deformation occurred during the fracturing for E = 5 GPa. It is also concluded that for given fixed confining pressures, the calculated J-integral value increases as the stiffness of the sandstone increases.

The results show a significant increase in apparent fracture toughness, which rises to be up to 7 times larger than at low confinement stress. The positive relationship between cracking driving force and applied stresses were plotted. This can be derived into failure assessment diagrams (FAD) so that the highly nonlinear elastic-plastic fractures can be presented by parameters that vary linearly with applied loads. By implementing assessment points, simple engineering judgement can be made based on FAD.

REFERENCES

Anderson, TL. 2017. “Fracture Mechanics: Fundamentals and Applications”. CRC Press.

Carrier, B, and S Granet. 2012. “Numerical Modeling of Hydraulic Fracture Problem in Permeable Medium Using Cohesive Zone Model.” Engineering Fracture Mechanics, Volume 79, p. 312–28.

Chen, Z. 2013. “An ABAQUS Implementation of the XFEM for Hydraulic Fracture Problems.” In Effective and Sustainable Hydraulic Fracturing. InTech, p. 725-739.

Clifton, R, and A Abou-Sayed. 1981. “A Variational Approach to the Prediction of the Three-Dimensional Geometry of Hydraulic Fractures.” In SPE/DOE Low Permeability Gas Reservoirs Symposium. Denver, Colorado: Society of Petroleum Engineers.

Cundall, PA, and ODL Strack. 1979. “A Discrete Numerical Model for Granular Assemblies.” Geotechnique, Volume 29, Issue 1, p. 47-65.

Damjanac, B, I Gil, M Pierce, M Sanchez, A Van As and J McLennan. 2010. “A New Approach to Hydraulic Fracturing Modeling In Naturally Fractured Reservoirs,” January. American Rock Mechanics Association.

D. W. Hu, H. Zhou, F. Zhang, and J. F. Shao, “Evolution of poroelastic properties and permeability in damaged sandstone,” *International Journal of Rock Mechanics and Mining Sciences*, vol. 47, no. 6, pp. 962–973, Sep. 2010, doi: 10.1016/j.ijrmms.2010.06.007.

Economides, MJ, and Nolte, KG. 2000. “Reservoir Stimulation.” John Wiley & Sons, UK.

F. Guot, N. R. Morgenstern:~, and J. D. Scott, “Interpretation of Hydraulic Fracturing Breakdown Pressure,” 1993.

Gordeliy, E, and A Peirce. 2013. “Coupling Schemes for Modeling Hydraulic Fracture Propagation Using the XFEM.” Computer Methods in Applied Mechanics and Engineering, Volume 253, p. 305–322.

H. Abass and C. Lamei, “Hydraulic Fracturing: Experimental Modeling,” in *Hydraulic Fracture Modeling*, Elsevier Inc., 2018, pp. 431–489.

H. Song and S. S. Rahman, “An extended J-integral for evaluating fluid-driven cracks in hydraulic fracturing,” *Journal of Rock Mechanics and Geotechnical Engineering*, vol. 10, no. 5. Chinese Academy of Sciences, pp. 832–843, Oct. 01, 2018, doi: 10.1016/j.jrmge.2018.04.009.

Irwin, GR. 1957. “Analysis of Stresses and Strains near the End of a Crack Traversing a Plate.” Journal of Applied Mechanics.

J. F. Hazzard, R. P. Young, and S. J. Oates, “Numerical modeling of seismicity induced by fluid injection in a fractured reservoir.”

J. R. Rice, “A Path Independent Integral and the Approximate Analysis of Strain Concentration by Notches and Cracks,” 1968.

Khristianovic, S, and Y Zheltov. 1955. “Formation of Vertical Fractures by Means of Highly Viscous Fluids.” p. 579–86. Rome, Italy: 4th World Petroleum Congress, 6-15 June, Rome, Italy.

Kresse, O, X Weng, H Gu, and R Wu. 2013. “Numerical Modeling of Hydraulic Fractures Interaction in Complex Naturally Fractured Formations.” Rock Mechanics and Rock Engineering, Volume 46, Issue 3, p. 555–568.

Lecampion, B. 2009. “An Extended Finite Element Method for Hydraulic Fracture Problems.” Communications in Numerical Methods in Engineering, Volume 25, Issue 2, p. 121–133.

Liu, D, B Lecampion, and L Benedetti. 2017. “Modeling of the Propagation of Hydraulic Fracture Using Cohesive Zone Models.” Computers and Geotechnics, Volume 91, p. 58-70.

Meyer, BR, and LW Bazan. 2011. “A Discrete Fracture Network Model for Hydraulically Induced Fractures - Theory, Parametric and Case Studies.” In SPE Hydraulic Fracturing Technology Conference. Society of Petroleum Engineers.

M. Yu, C. Wei, L. Niu, S. Li, and Y. Yu, “Calculation for tensile strength and fracture toughness of granite with three kinds of grain sizes using three-point-bending test,” *PLoS ONE*, vol. 13, no. 3, Mar. 2018, doi: 10.1371/journal.pone.0180880.

P. A. Cundall and D. L. St, “A discrete numerical model for granular assemblies,” 1979.

Perkins, TK, and L Kern. 1961. “Widths of Hydraulic Fractures.” Journal of Petroleum Technology, Volume 13, Issue 9, p. 937–949.

Potyondy, DO, and PA Cundall. 2004. “A Bonded-Particle Model for Rock.” International Journal of Rock Mechanics And Mining Sciences, Volume 41, Issue 9, p. 1329-1364.

Qingwen, R, D Yuwen, and Y Tiantang. 2009. “Numerical Modeling of Concrete Hydraulic Fracturing with Extended Finite Element Method.” Science in China Series E: Technological Sciences, Volume 52, Issue 3, p. 559–565.

S. Costa, J. Kodikara, and J. Xue, “J-integral as a useful fracture parameter for analysis of desiccation cracking in clayey soils,” in *Coupled Phenomena in Environmental Geotechnics: From Theoretical and Experimental Research to Practical Applications - Proceedings of the International Symposium, ISSMGE TC 215*, 2013, pp. 377–381, doi: 10.1201/b15004-46.

Shlyapobersky, J. 1985. “Energy Analysis of Hydraulic Fracturing.” In The 26th U.S. Symposium on Rock Mechanics (USRMS), 26-28 June, Rapid City, South Dakota, ARMA-85-0539-1.

S. N. Atlurit, T. Nishiokat, and M. Nakagaki, “Incremental path-independent integrals in inelastic and dynamic fracture mechanics,” 1984.

S. Su and Y. Che, “Applying condition of Kirsch’s stress solution for plate with central hole in the engineering,” in *Applied Mechanics and Materials*, 2012, vol. 166–169, pp. 3012–3017, doi: 10.4028/www.scientific.net/AMM.166-169.3012.

Vahab, M, and N Khalili. 2018. “X-FEM Modeling of Multizone Hydraulic Fracturing Treatments Within Saturated Porous Media.” Rock Mechanics and Rock Engineering, p. 1–21.

Valkó, P, and MJ Economides. 1995. Hydraulic Fracture Mechanics. Wiley.

W. Hua, J. Li, S. Dong, and X. Pan, “Experimental study on mixed mode fracture behavior of sandstone underwater-rock interactions,” *Processes*, vol. 7, no. 2, Feb. 2019, doi: 10.3390/pr7020070.

Wang, HY. 2015. “Numerical Modeling of Non-Planar Hydraulic Fracture Propagation in Brittle and Ductile Rocks Using XFEM with Cohesive Zone Method.” Journal of Petroleum Science and Engineering, Volume 135, p. 127–140.

Warpinski, N, P Branagan, and R Wilmer. 1985. “In-Situ Stress Measurements at US DOE’s Multiwell Experiment Site, Mesaverde Group, Rifle, Colorado.” Journal of Petroleum Technology, Volume 37, Issue 3, p. 527–536.

X. Zhao and R. Paul Young, “Numerical modeling of seismicity induced by fluid injection in naturally fractured reservoirs,” *Geophysics*, vol. 76, no. 6, 2011, doi: 10.1190/geo2011-0025.1.

Yang, Y, X Tang, H Zheng, Q Liu, and Z Liu. 2018. “Hydraulic Fracturing Modeling Using the Enriched Numerical Manifold Method.” Applied Mathematical Modelling, Volume 53, p. 462–86.

Yew, CH. 1997. Mechanics of Hydraulic Fracturing. Gulf Professional Publishing.

Y. Liu and M. Amro Professor, “Modeling Shale Rock Behavior Using a Flat Joint Model.”